Boundary-Layer Meteorol (2007) 123:481–509
DOI 10.1007/s10546-007-9156-y

ORIGINAL PAPER

Filtering of windborne particles by a natural windbreak

Thomas Bouvet · Benjamin Loubet · John D. Wilson · Andree Tuzet

Received: 22 February 2006 / Accepted: 30 December 2006 / Published online: 17 February 2007

Abstract New measurements of the transport and deposition of artificial heavy particles (glass beads) to a thick 'shelterbelt' of maize (width/height ratio $W/H \approx 1.6$) are used to test numerical simulations with a Lagrangian stochastic trajectory model driven by the flow field from a RANS (Reynolds-averaged, Navier–Stokes) wind and turbulence model. We illustrate the ambiguity inherent in applying to such a thick windbreak the pre-existing (Raupach et al. 2001; Atmos. Environ. **35**, 3373–3383) 'thin windbreak' theory of particle filtering by vegetation, and show that the present description, while much more laborious, provides a reasonably satisfactory account of what was measured. A sizeable fraction of the particle flux entering the shelterbelt across its upstream face is lifted out of its volume by the mean updraft induced by the deceleration of the flow in the near-upstream and entry region, and these particles thereby escape deposition in the windbreak.

Keywords Filtering · Flux and concentration measurements · Heavy particle · Lagrangian Stochastic model · Maize shelterbelt · RANS wind flow model · Windbreak

T. Bouvet · B. Loubet · A. Tuzet
Unité mixte de recherche 'Environnement Grandes Cultures' INAPG-INRA,
Thiverval-Grignon, France

T. Bouvet (✉) · J. D. Wilson
Department of Earth & Atmospheric Sciences, University of Alberta,
1-26 Earth Sciences Building, Edmonton,
Alberta, Canada T6G 2E3
e-mail: bouvet.thomas@gmail.com

List of symbols and acronyms

$(\overline{\ })$	Time averaged quantity
ϵ	Dissipation rate of the turbulent kinetic energy
η	Optical porosity
θ	Wind direction
ρ	Air density
σ	Particle transmittance across a windbreak
σ_x	Standard deviation in the quantity x
τ_p	Particle Stokesian time scale
τ_{ij}	Reynolds stress tensor
Ω	Speed of rotation
A	Vegetation area density
c	Particle concentration
C_d	In-situ drag coefficient of vegetation
d_p	Particle diameter
e	Coefficient of velocity restitution upon rebound
E_I	Efficiency of impaction
F_i	Particle flux across a boundary of the shelterbelt
g	Gravitational acceleration
H	Windbreak height
H_s	Particle source height
k_v	Von Karman constant
L_mo	Obukhov length
L_v	Length scale of a vegetation element
m	Meandering factor
P_I	Probability of particle interception
Q	Particle source intensity
Q_h	Heat flux density
R_i	Experimental run label
Re	Reynolds number
s	Horizontal wind speed
S_t	Stokes number
t	Time
T_L	Lagrangian integral time scale
u	Wind velocity in the direction normal to the windbreak
u_p	Particle velocity in the direction normal to the windbreak
$u_\star$	Friction velocity
v	Wind velocity in the direction parallel to the windbreak
v_p	Particle velocity in the direction parallel to the windbreak
V_b	Bleed velocity through a screen
V_c	Critical velocity of rebound
V_i	Particle impact velocity
V_r	Particle rebound velocity
W	Windbreak thickness
w	Wind velocity in the vertical direction
w_p	Particle velocity in the vertical direction
w_g	Particle gravitational settling velocity

x	Distance in the direction normal to windbreak
X_s	Position of the source in the horizontal
y	Distance in the direction parallel to windbreak
z	Height
z_0	Roughness length

1 Introduction

Bouvet et al. (2006) provided new measurements of the deposition of heavy particles in disturbed micrometeorological flow, specifically in the region of a thin artificial windbreak. Comparative simulations, using a first-order Lagrangian Stochastic (LS) trajectory model coupled with a Reynolds-averaged, Navier–Stokes (RANS) second-order closure wind and turbulence model, reproduced satisfactorily (within a 30% root-mean-square error) the mean features of the deposition swath, i.e., its overall shape and horizontal extent, and the location and intensity of the deposition peak. Here we extend that investigation by addressing the case where the windbreak not only perturbs the mean streamlines of the airflow carrying the particles, but also filters the passing airstream. We address the case of a thick, natural windbreak, with a focus on particle transport and deposition *inside* the vegetation. The general context of the project is the use of windbreaks to control the drift and deposition of sizeable particles near ground, an environmental manipulation with a long history (and probably indeed *pre*-history) in relation to soil erosion[1](Dong et al. 2000), and which is familiar now in the form of highway fences to control snow drift (Shaw 1988). A comprehensive understanding of windbreaks is demanded if we wish to engineer their use to control, for instance, the off-target drift of pesticides (Woods et al. 2001), minimize genetical pollution of the environment by modified genes carried by wind-blown pollen (Klein et al. 2003), or mitigate the spread of pathogenic agents (Waggoner and Taylor 1958, Aylor 1990). Furthermore in these contexts it is clear that a good process-based understanding on micrometeorological time scales (circa 30 min) does not entirely suffice, for the role of extreme events (to take but one example, thunderstorm gust fronts), which almost by definition it is difficult to incorporate, may be a critical one.

Regarding the present state of our knowledge in regard to windbreaks as airstream 'filters', Raupach et al. (2001) provided an interesting and useful analysis for the restricted case of a 'thin windbreak', specifically where the ratio W/H of windbreak width (W, alongstream) to height H is so small that variation of wind speed across the windbreak can be neglected. These authors were able to relate the ratio $\sigma = \overline{c}_2/\overline{c}_1$ of particle mean concentrations immediately downwind ($\overline{c}_2$) and upwind ($\overline{c}_1$) of the fence to the optical porosity of the windbreak:[2] evidently if $V_b(z)$ is the bulk mean wind speed 'at' the thin windbreak (the 'bleed' velocity) then

$$D = V_b\,(\overline{c}_1 - \overline{c}_2) = V_b\overline{c}_1\,(1-\sigma) \tag{1}$$

is the local rate of filtration of particles by the windbreak (in Sect. 4.4, we will schematically apply this model to the present experiments). This is a good beginning, but it remains to work out a useable treatment of natural (thick) hedges and

[1] Taking the global view, soil degradation caused by wind erosion has affected about 5 million km^2 of land surface, or over 40% of the total of degraded lands (Oldeman et al. 1991).

[2] Throughout this paper subscripts 0, 1, 2 will, respectively, designate properties measured far upwind from the shelterbelt (0), along its upstream face (1), and along its downstream face (2).

shelterbelts, which are regarded (Maber 1998) as more efficient particle traps than artificial thin windbreaks. As vegetation elements are obstacles to particles, a thick natural shelterbelt constitutes, in essence, a multiple impactor. There is an engineering literature regarding such types of filters, largely focused around specification of a bulk filtering efficiency factor (e.g., Shaw 1978) as a function of the thickness of the filter, the trapping efficiency of a single trapping element, and the packing density of the filter. However these treatments do not carry over to the filtering of the wind by a natural windbreak, for the engineering models assume a steady and laminar (uniform) flow at entry to the filter. In short, the subject we address here has as yet received rather little attention (Ucar and Hall 2001).

In Sect. 2, we describe bead dispersion measurements about a natural thick shelterbelt, focusing on the vertical profiles of particle concentration and (streamwise) flux measured immediately upwind and downwind of a maize shelter belt, as well as the ground deposition flux within its boundaries; this study has many similarities with the work of Bouvet et al. (2006), indeed is identical as regards the experimental site and many aspects of the methodology. Section 3 describes a numerical model of shelterbelt filtration, and since the model is an extension of that described by Bouvet et al. (2006) (viz., LS trajectory model coupled to a RANS wind model), we shall emphasize what is different from the earlier work, namely the addition of an algorithm for deposition/rebound onto vegetation. In Sect. 4, we assess the capability of the RANS–LS model to mimic particle transport and deposition *inside* this natural windbreak, examine performance of the simpler 'thin windbreak' theory, and conclude by examining the (modelled) pattern of particle concentration and deposition across a wider region in proximity to the shelterbelt.

2 Particle entrapment by a shelterbelt: measured particle fluxes

As already noted, the present experiments were conducted in the same flat, even field of the earlier trials (Bouvet et al. 2006), amid short (0.1 m) stubble, while the 'windbreak', which stretched in a direction normal to the prevailing wind, was composed of four rows of maize: the row spacing was 0.8 m and the inter-plant spacing along the row was 0.15 m. At the time of the experiments the canopy height $H = 2.0 \pm 0.15$ m. As windbreak width $W \approx 3.2$ m, the aspect ratio $W/H \approx 1.6$, a value that (by design) should render inapplicable the thin-windbreak entrapment theory of Raupach et al. (2001). In what follows we define the origin of the streamwise axis ($x = 0$) to lie at the centre of the windbreak.

To provide information that would be needed by any theoretical description of deposition to leaves, the geometrical structure of the plants was measured by a FASTRAK three-dimensional digitizer (Polhemus 1993). The device consists of an electronic unit, a fixed-position electromagnetic field generator and a receiver that is pointed to the locations of measurements on the plant. The currents induced in the coils of the receiver allow retrieval of its position and orientation in the electromagnetic field. Each point measured is characterized by Cartesian co-ordinates (x, y, z) and Euler orientation angles (azimuth, elevation, roll angles). Sensing a random sample of plants in the shelterbelt allowed the estimate of the height distribution of leaf azimuth and zenith angles (Figs. 1, 2), as well as the 1-sided leaf area density (LAD) profile $A = A(z)$, in m^{-1}, and its (height-varying) projections onto the horizontal (A_{xy}) and vertical planes (A_{xz} and A_{yz}, respectively, perpendicular and parallel to

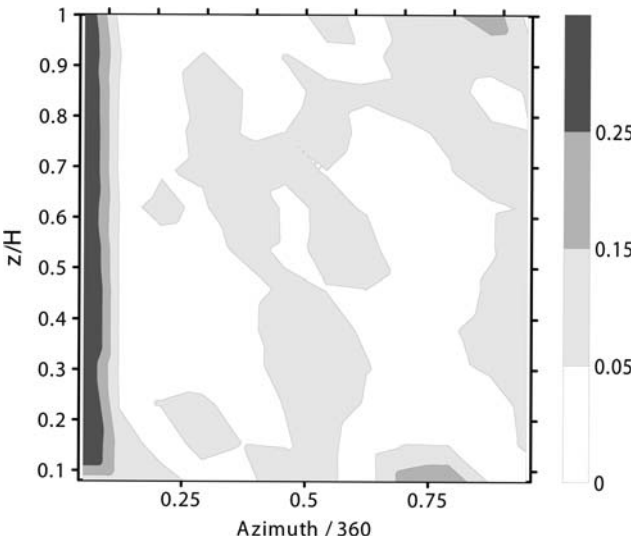

Fig. 1 Vertical profile of the leaf azimuthal angle distribution. The colour represents the proportion of leaves (measured by their area) across the azimuthal directions. Note that 0, 0.5 and 1 represent the direction perpendicular to the windbreak, whereas 0.25 and 0.75 represent the parallel

the hedge)[3], shown in Fig. 3. Note that the elevated minimum in the LAD profile at $z/H \approx 0.6$ reflects the observed situation of a combination of desiccated leaves at the base of the hedge hanging downward, and the healthier upper leaves pointing upward. The optical porosity $\eta(z)$, related to the frontal leaf area density as (Raupach et al. 2001) $\eta = \exp(-A_{yz}W)$ ranged from $\eta = 0.05$ where vegetation was very dense in the upper half of the windbreak, to $\eta = 0.67$ close to ground. Leaf dimensions were measured manually, on plants chosen randomly in each of the four rows, allowing us to achieve an independent estimate of the leaf area index. The latter proved to be highly consistent with the result derived from the digitalization measurements ($LAI = 3.54$ vs. $LAI = 3.52$).

During runs of 15-min duration, spherical glass beads of density $2,500\,\mathrm{kg\,m^{-3}}$, whose diameter d_p ranged from $10\,\mu\mathrm{m}$ to $50\,\mu\mathrm{m}$, were released from a 'line' source (see Bouvet et al. 2006) upwind from the windbreak. The particle size distribution at source was not known, but was however estimated at the entry face of the maize shelterbelt, as explained at the end of Sect. 2.2. At this location, about 50% of the particles lay in the range $20 < d_\mathrm{p} < 30\,\mu\mathrm{m}$, and particle median size was about $24\,\mu\mathrm{m}$. Five runs (labelled R1 to R5) were carried out, under the conditions described in Table 1. As detailed below, we measured the mean particle flux densities along the vertical faces of the maize belt, and the deposition flux to ground within the windbreak. The configuration of the experiments is sketched in Figs. 4–5. In runs R1 and R2, the measurements were split into two particle size ranges: 10–25 $\mu\mathrm{m}$ and 30–50 $\mu\mathrm{m}$, labelled, respectively, with suffixes 'a' and 'b' (R1a, R1b, R2a, R2b).

[3] The subscripts x, y and z denote, respectively, the direction perpendicular to the hedge, parallel to the hedge and the vertical; the double subscript notation xy refers to the orientation of a surface whose normal is vertical, i.e., a horizontal surface, (etc).

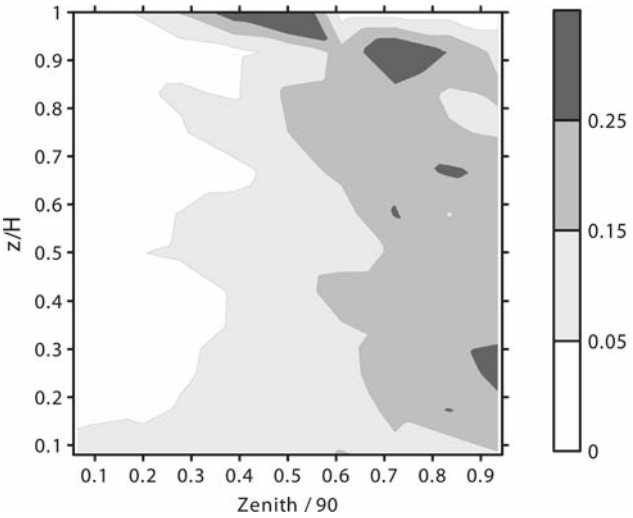

Fig. 2 Vertical profile of the leaf zenithal angle distribution. The colour represents the proportion of leaves (measured by their area) across the zenithal directions. Note that 0 represents the horizontal, whereas 1 represents the vertical direction

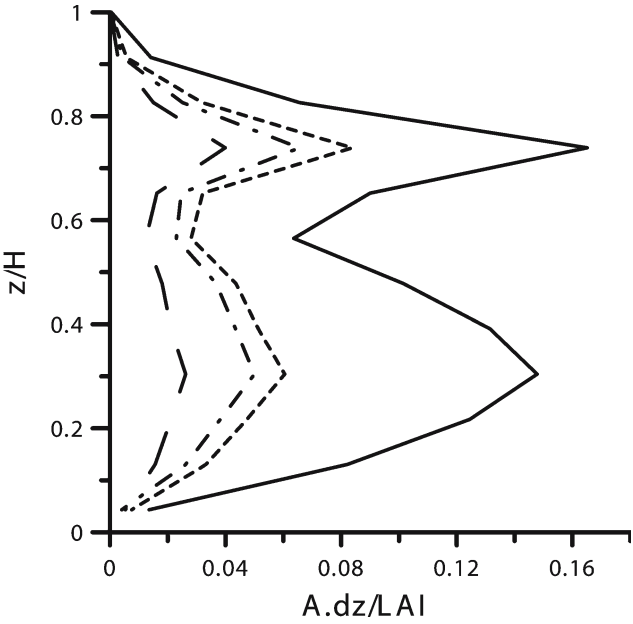

Fig. 3 Vertical profile of vegetation leaf area density $A(z)$ (solid curve) and its projections $A_{xy}(z)$ (short dashed curve), $A_{xz}(z)$ (long dashed curve), $A_{yz}(z)$ (dashed dotted curve), normalized by the leaf area index (LAI)

Table 1 Conditions of experimental runs

Run label	Source height (normalized by the Hedge's height)	Micrometeorology				
		Mean wind direction θ_0(°)	Standard deviation of wind direction θ_0(°)	Friction velocity u_{*0} (m s^{-1})	Obukhov length L_{mo} (m)	Roughness length z_0 (m)
R1	0.91	−33.5	9.6	0.27	−19.8	0.02
R2	0.91	−25.0	16.8	0.14	−1.8	0.01
R3	0.91	−49.5	16.0	0.29	−101.0	0.01
R4	0.91	22.2	25.6	0.34	−28.8	0.01
R5	1.06	−38.5	10.0	0.22	−74.2	0.02

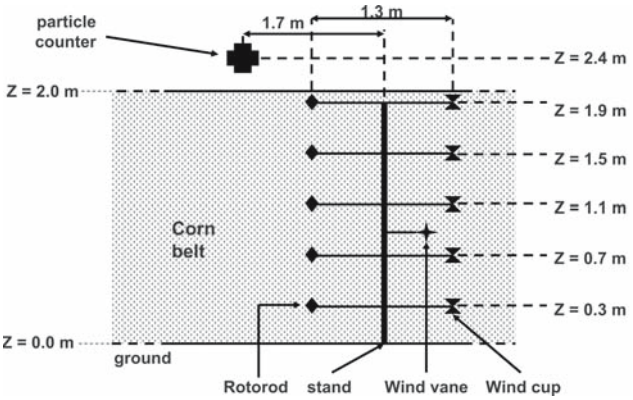

Fig. 4 Frontal view of the experimental set-up

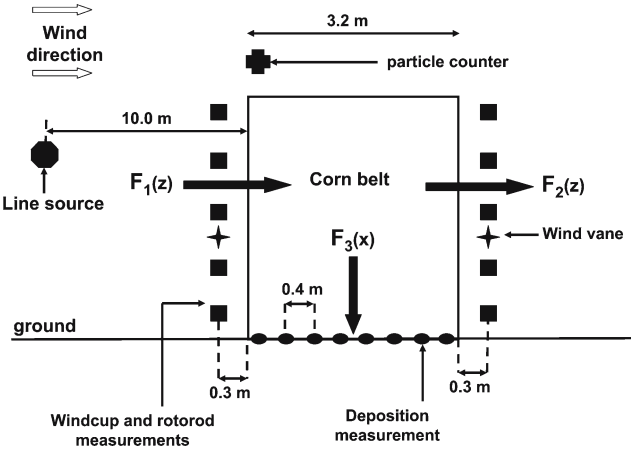

Fig. 5 Side view of the experimental set-up

2.1 Host flow

Cup wind speed ($s = \sqrt{u^2 + v^2}$) and temperature were measured at six levels (0.6, 1.1, 2.0, 3.0, 4.5, 6.0 m) in the undisturbed flow at a distance of 72.5 m upwind from

the windbreak, where the Monin–Obukhov similarity theory applies (CIMEL CE155 cup anemometers, operating range 0.3–50.0 m s^{-1}; shielded and ventilated Copper-Constantan thermocouples). In addition, the approaching wind direction (θ_0) was measured with a wind vane (MCB, Courbevoie, France).

Statistics of the host flow, namely friction velocity ($u_\star$), mean vertical heat flux density (Q_h), aerodynamic roughness length (z_0), mean ($\overline{\theta_0}$) and standard deviation ($\sigma_{\theta 0}$) of the wind direction, were computed over the lapse of each experimental run (15 min) from those measurements. Methods of calculation are provided in Sect. 4.1. Independent estimates of $u_\star$ and Q_h were available from a three-dimensional ultrasonic anemometer (type R3, Gill) placed 4 m above the ground, upwind in the approach flow.

2.2 Particle concentrations and fluxes

Figure 4 shows the three (of four) particle exchange fluxes (F_1, F_2, F_3) to/from the shelterbelt volume, which we were able to determine from the experimental runs. $F_1(z) = \overline{u}_1(z)\,\overline{c}_1(z)$ and $F_2(z) = \overline{u}_2(z)\,\overline{c}_2(z)$ estimate the horizontal fluxes of particles transported by the mean wind across (respectively) the upwind and downwind side boundaries of the maize belt, and were evaluated (only) 0.3 m from the sides of the maize belt, at levels $z/H = (0.15,\ 0.35,\ 0.55,\ 0.75,\ 0.95)$. At these faces the mean horizontal velocity component $\overline{u}$, defined as the component perpendicular to the windbreak, was estimated from local cup wind speed (s) and wind direction (θ) measurements performed with the same instruments as in the upwind flow, with

$$\overline{u} = \overline{s}\cos(\overline{\theta}). \tag{2}$$

Mean concentration $\overline{c}$ was measured using particle trapping instruments based on the design of Jarosz et al. (2003), and resembling the commercial instrument known as the 'rotorod'. As shown on Fig. 6, these instruments consisted of spinning arms that trapped particles whose inertia prohibited their escape from the swept-out volume. Each trap was composed of a 2-mm square-section brass rod, bent into a U-shape to give two vertical arms, these being 50 mm long and spaced by a distance $D = 80$ mm apart. The arms were mounted to 1.2 V (DC) electric motors so as to rotate at about $\Omega = 300$ rpm (note: Ω was determined specifically for each individual trap) and sample about 15 l of air per minute. It so happened that for the specific conditions of the experiments, viz. particle release rate Q, position of detectors relative to source,

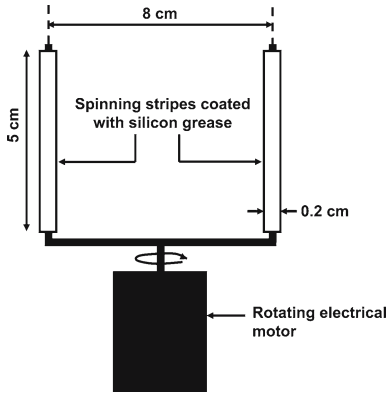

Fig. 6 Schematic of the particle trap instrument

15-min integration, $15\,\mathrm{l\,min^{-1}}$ represented a sampling rate that yielded a statistically satisfactory count (small ratio of standard deviation to mean number of particles per unit area of the trapping surface), while avoiding saturation (i.e., too many beads captured, with resulting ambiguity as to collection efficiency). Particles lying in the volume swept out by the rotating arms were deposited onto plastic strips (dimension $w \times h = 2 \times 50\,\mathrm{mm}^2$) attached to the arms, these strips being coated with a thin layer of silicon grease to ensure the intercepted particles remained stuck. After each run, the sample strips were detached and mounted on a microscope slide for visual counting with a light microscope. In order to alleviate the workload associated with the counting, bead counts were made on a sub-sample area (about 25% of the total surface of the strips) with the aid of a stencil scribed evenly with 10 slots of 0.45-mm width each and placed over the slide. Thereby we achieved a systematic sampling that allowed us to account for heterogeneity of the bead distribution on the strips. The average particle concentration, $\overline{c}$ was determined as

$$\overline{c} = \frac{N_\mathrm{p}}{2\,w\,h\,\Omega\,\pi\,D\,\Delta t E_\mathrm{I}} \tag{3}$$

where N_p is the number of particles counted on the two arms of each trap, Δt is the duration of an experimental run and E_I is the efficiency of impaction of the particles on the arms, calculated according to Aylor's (1982) fit to May and Clifford's (1967) data for impaction on a cylinder:

$$E_\mathrm{I} = \frac{0.86}{1 + 0.442\,S_t^{-1.967}}, \tag{4}$$

where $S_t = |v|\tau_\mathrm{p}/L$ is the Stokes number of the particle to the impactor and $L = 2\,\mathrm{mm}$ is the characteristic length of this impactor. With a rotational speed of 300 rpm, $27\% \le E_\mathrm{I} \le 86\%$ when $10 \le d_\mathrm{p} \le 50\ \mu\mathrm{m}$, i.e. E_I is highly sensitive to the particle diameter. In runs R1 and R2, the optical count was split into a class of small beads ($10 \le d_\mathrm{p} \le 25\ \mu\mathrm{m}$) and a class of large beads ($30 \le d_\mathrm{p} \le 50\ \mu\mathrm{m}$). For the other runs, no size class distinction was attempted, and all beads with diameter $10 \le d_\mathrm{p} \le 50\ \mu\mathrm{m}$ were counted.

The deposition flux F_3 was sampled on ground at eight locations (spaced 0.4 m apart) across the maize belt, as indicated on Fig. 5. As in the earlier trials (Bouvet et al. 2006) depositing particles were collected in electrolyte-filled Petri dishes and enumerated by a liquid phase spectral counter (Multisizer Coulter Counter®, Beckman Coulter Inc., 4- μm diameter resolution). Unfortunately these electrolyte samples proved to be heavily polluted by alien particles in the range of diameters $d_\mathrm{p} \le 20\ \mu\mathrm{m}$, and we were able to extract a meaningful deposition rate only for runs R1, R2 for the aggregate size class $30 \le d_\mathrm{p} \le 50\ \mu\mathrm{m}$. The deposited samples did however prove useful in another role: together with measurements of particle concentration at the top of the windbreak, where was operated an FM-100 particle spectrometer (Droplet Measurement Technologies, Inc., Boulder, CO, USA), they allowed us to estimate (by interpolation) the particle size distribution at heights intermediate between ground and the top of the windbreak.

3 Theoretical model of particle filtration

3.1 Resolved scales of motion

For comparison with the experiments, theoretical particle dispersion statistics (concentration field, flux field) were derived from an ensemble of computed particle trajectories, using the LS model described by Bouvet et al. (2006), to which it was necessary to add an algorithm parameterizing capture by leaves (see below). The LS model was driven by a synthetic wind flow computed specifically for each experimental run documented in Table 2, over a domain having $266H$ streamwise and $55H$ vertical extent.

It would be redundant to elaborate on the wind model, described and tested in some detail by Wilson et al. (2001) and Wilson (2004). Suffice to say that it was a Reynolds-averaged Navier–Stokes (RANS) wind model based on the second-order turbulent closure of Rao et al. (1974). It provided a disturbed field of all velocity statistics up to the second order, that is, fields of mean velocity, Reynolds stress τ_{ij}, and turbulent kinetic energy dissipation rate ϵ. The inflow profiles of the velocity statistics were specified as the one-dimensional (1D) equilibrium solution consistent with the measured (see Sect. 2.1) approach flow state and orientation ($u_\star$, Obukhov length L_{mo}, z_0, $\overline{\theta}$). Note that the modelled flow statistics accounted for both the obliquity of the wind flow to the hedge and the thermal stratification of the air. The profile of the effective drag coefficient $c_{\mathrm{d}}(z)$ was tuned for a best match with the measured profiles of the mean wind $\overline{u}_1(z), \overline{u}_2(z)$ at the entry and exit faces of the shelterbelt. The impact of $c_{\mathrm{d}}(z)$ on the flow model is through localized sinks for mean horizontal momentum and velocity variance, symbolically

$$\frac{\partial \overline{u}}{\partial t} \propto -c_{\mathrm{d}}(z)\, A_{yz}(x,z)\, \overline{u} \sqrt{\overline{u}^2 + \overline{v}^2} \tag{5}$$

$$\frac{\partial \sigma_u^2}{\partial t} \propto -c_{\mathrm{d}}(z)\, A_{yz}(x,z)\, \overline{u}\, \sigma_u^2 \tag{6}$$

where within the shelter $A_{yz}(x,z) \equiv A_{yz}(z)$, the leaf area density profile, while outside the shelter $A_{yz}(x,z) = 0$. As one expects, the momentum sinks oppose the flow (cf. negative sign) and are sensitive to vegetation density and wind velocity (for further justification of Eqs. 5–6, see Wilson 2004). By adjusting $c_{\mathrm{d}}(z)$[4] we were able to achieve a reasonably close match between the modelled and the measured horizontal velocity components $\overline{u}$, $\overline{v}$ at heights $z/H = (0.15, 0.35, 0.55, 0.75, 0.95)$ immediately upwind and downwind of the belt.

Particle trajectories were computed using the simplified approach (Wilson 2000) wherein, in essence, a gravitational settling velocity w_{g} is merely superposed on what would otherwise be the trajectory of a fluid element. Thus particle inertia is not explicitly represented, and particle velocity variance is assumed to equal fluid velocity variance. Because trajectories are terminated at the ground, Wilson (2000) called this approach (which had already been widely used) the 'Settling Sticky Fluid Element' method. For small enough values of the ratio $\tau_{\mathrm{p}}/T_{\mathrm{L}}$ of the particle's inertial (i.e., Stokesian) time constant to the integral scale of the driving turbulence, these approximations were proven to be acceptable. In our experimental conditions, assuming the

[4] The optimal profiles of $c_{\mathrm{d}}(z)$ yielded values in the range 0.6–1.8. Smaller values were coincident with lower heights and wind speed, as previously reported by Finnigan (2000).

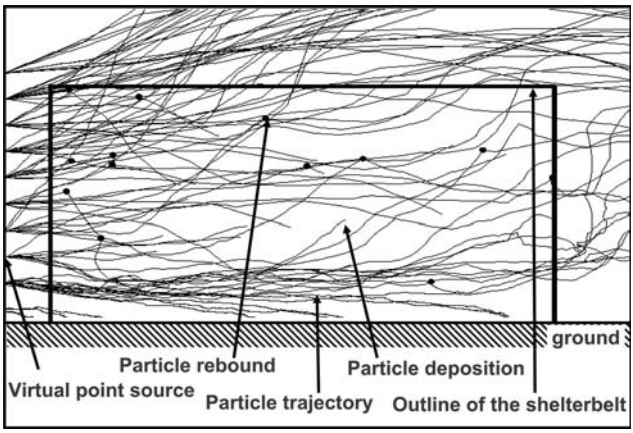

Fig. 7 Side view of numerically simulated particle trajectories across the shelterbelt

shelterbelt acts on the flow as a diffuse momentum sink (the flow about the vegetation elements is not resolved), the condition $\tau_p/T_L << 1$ is met for all particles in the range 10–50 μm except in the lowest 0.2 m above the ground.

The carrier fluid velocity was calculated using Thomson (1987) well-mixed multi-dimensional algorithm for Gaussian inhomogeneous turbulence, with an adjustment to the effective Lagrangian decorrelation time scale to account for the crossing trajectory effect (Csanady 1963). Raupach (2002) gave experimental evidence for the utility of this adjustment. Velocity statistics required by the LS model (thus, provided by the RANS wind model) were the mean velocities, the Reynolds stress tensor τ_{ij}, and the turbulent kinetic energy dissipation rate ϵ. They were linearly interpolated (with distance) from the values computed by the wind-flow model at the four nearest grid points. As an illustration, Fig. 7 shows a side view of trajectories simulated by the LS model in the meteorological conditions of run R5.

3.2 Modelling of a virtual source

The reader will notice on Fig. 7 that particles commenced their (imaginary) journeys from discrete locations slightly upwind from the hedge. This is because the particle size distribution was unknown at source (and in turn the source intensity for specific diameter classes was unknown, also), the actual (single) crosswind line source (at $z/H = 0.82$ or 0.95; $x/W = -3.6$) could not be simulated. Instead it was represented for the computation by ten 'virtual' crosswind line sources at heights $z/H =$ (0.05, 0.15, 0.25, 0.35, 0.45, 0.55, 0.65, 0.75, 0.85, 0.95) lying at $x/W = -0.60$. The intensity of those line sources was determined so as to reproduce the measured particle concentration profile upwind of the hedge, according to

$$Q_j = \overline{c}_j \, dZ_j \, \overline{u}_j. \tag{7}$$

Here Q_j is the needed line source intensity at level j, $\overline{u}_j$ is the component of the mean horizontal velocity perpendicular to the hedge (as computed by the RANS model), and dZ_j is the height of the bin over which the concentration $\overline{c}_j$ is averaged (note: in reality the concentration was only measured at $z/H = (0.15, 0.35, 0.55, 0.75, 0.95)$, and we interpolated linearly to intermediate levels). Each particle released in the

LS model was assigned a diameter (and corresponding inertial time scale) consistent with the particle size distribution at the level of the virtual source. As in truth the physical particles were released further upwind than $x/W = -0.6$, the particle size distribution had time to evolve so as to become non-uniform along the vertical, by the time particles reached the virtual (computational) source plane. The particle size distribution was estimated at each level of the virtual source by linear interpolation (with respect to distance) between the distributions observed at $x/W = -0.6$ on ground (as measured with the liquid phase counter of deposited particles) and at $z/H = 1.2$ (as measured with the FM-100 instrument). Note also that enforcing the correct (measured) concentration entry profile allowed us to focus on testing the skill of the transport and deposition model specifically *inside* the shelterbelt.

3.3 Parameterization of deposition and rebound on leaves

Along its trajectory across the maize belt a particle likely would have encountered stems and leaves on which it might deposit. The probability of deposition depends on the probability that the particle will 'encounter' a vegetation element,[5] and (multiplicatively) on the probability of capture subsequent to or conditional on encounter. Following the approach of Wilson (2000) and Aylor and Flesch (2001), we expressed the probability of particle impingement P_I on vegetation over a timestep dt as

$$P_\mathrm{I} = (u_\mathrm{p}\, A_{yz}\, E_{\mathrm{I},yz} \;+\; v_\mathrm{p}\, A_{xz}\, E_{I,xz} \;+\; w_\mathrm{p}\, A_{xy}\, E_{\mathrm{I},xy})\ \mathrm{d}t \tag{8}$$

where $(u_\mathrm{p}, v_\mathrm{p}, w_\mathrm{p})$ is the particle velocity (which, note, we regard as 'resolved' in the model, whereas the motion carrying the particle onto or around an impediment such as a leaf remains unresolved) and E_I is the efficiency of interception by impaction or sedimentation. We assumed that the efficiency of interception of particles settling under gravity was total ($E_{\mathrm{I},xy} = 1$),[6] and estimated the efficiencies of impaction $E_{\mathrm{I},xz}, E_{\mathrm{I},yz}$ according to Eq. 4 where $S_t = |v|\tau_p/L_\mathrm{v}$ is the Stokes number of the particle in relation to the vegetation element and L_v is the characteristic size of a vegetation element. We defined the latter as the width of a maize leaf projected on the plane perpendicular to the particle's trajectory. From LS simulations, we found an average value of $L_\mathrm{v} \approx 0.02$ m.

After impact upon a surface, a particle may rebound. As Dahneke (1971, 1975) describes in his analysis of the energy balance of particles impinging and rebounding on a surface, particles lose energy from adhesion forces and by plastic deformation of the particle and/or the surface. Rebound will occur if the kinetic energy at impact is large enough to overcome the loss of energy. Paw U (1983) showed that the theory of Dahneke (1975) adequately describes experiments with natural and artificial particles (glass beads, lycopodium spores and ragweed pollen of diameter) impinging on natural and artificial surfaces (Tulip poplar leaves, American elm leaves or glass). According to those experimental results, particles rebound if the velocity component perpendicular to the impinging surface before impact is above a 'critical rebound velocity'. For 30 μm (d_ref) glass beads, he reported a critical velocity $V_\mathrm{c}(d_\mathrm{ref}) = 0.28\,\mathrm{m\,s^{-1}}$. To account for the influence of particle diameter (d_p) on the critical velocity ($V_\mathrm{c} \propto d_\mathrm{p}^{-3/2}$

[5] An 'encounter' is defined as the event of a trajectory segment, computed in the 'resolved flow' as if vegetation were not present, crossing a leaf or stem.

[6] Gravitational settling alone guarantees that a particle encountering a horizontal surface will be intercepted, regardless of the efficiency of deposition due to turbulent motion itself.

according to the theory of Dahneke 1975), we adjusted in the model the experimental value of Paw U as

$$V_c(d_p) = V_c(d_{ref}) \left(\frac{d_{ref}}{d_p} \right)^{3/2}. \quad (9)$$

Interestingly, Paw U (1983) showed that this critical velocity is approximately constant regardless of the surface type. Therefore, we assumed that Eq. 9 was applicable in our conditions (glass beads impinging on maize leaves) and invoked it in the trajectory model. The ratio of the rebound velocity V_r to the impaction velocity V_i (known as the coefficient of restitution, e) also depends on the impaction velocity. Obviously, $V_r/V_i = 0$ as long as $V_i \leq V_c$; as V_i passes and exceeds V_c, V_r/V_i soars and levels off quickly. The plateau value proves to be very similar across surface types, and on average $e = 0.82$ for glass beads. It is assumed in our model that

$$V_r = 0.82 V_i \quad (10)$$

when $V_i > V_c$. According to Xu and Willeke (1993), both the critical rebound velocity and the velocity of rebound depend strongly on the angle of incidence of the particle to the surface. In the experiment of Paw U (1983), the impactor used was a cylinder of glass wrapped with various types of leaves, so those results pertain to particles impinging and rebounding on surfaces with various angles of incidence, as in the case of our experiment. Therefore, we assumed Paw U's results are directly applicable to our situation. Note that the parameters characterizing the vegetation, which are involved in the equations describing deposition and rebound (Eqs. 8–10), were measured experimentally as mentioned in Sect. 2: the maize belt was characterized by digitalization measurements capturing the architecture of vegetation along a vertical profile (split into 13 vertical levels along the height of the hedge), in terms of the plant area density (m^{-1}) and its projections onto each of the three directions, and the leaf orientation distribution (azimuth and zenith). The dimensions of the leaves (measured manually) were used in the calculation of the Stokes number St in Eq. 4. It is also worthwhile noting that the wide range in particle size ($10 < d_p < 50$ μm) leads to variations in the impaction efficiencies, critical rebound velocity and gravitational settling velocity by respectively a factor of (at most) 200, 10, 25. Consequently a proper description of particle filtration (i.e., phenomena of gravitational settling on horizontal surfaces, impaction and rebound) requires to explicitly account for particle size distribution, as done in the present model (cf. Eqs. 4 and 9). However the strong sensitivity to particle size makes the model very prone to errors due to inaccuracies in the estimated particle size distribution. For example, overestimating the diameter of a 25 μm particle as 30 μm would lead to overestimating its gravitational settling velocity and impaction efficiency by, respectively, 30% and 45%, while underestimating its critical rebound velocity by 25%.

4 Results

4.1 Micrometeorology of the host flow

Estimates of the friction velocity ($u_\star$) and heat flux (Q_h) were achieved by best-fitting the temperature and velocity vertical profiles predicted by the Monin–Obukhov similarity theory (MOST) to the corresponding measurements. They were consistent with

Table 2 Micrometeorological conditions computed from the sonic anemometer measurements and the temperature and wind velocity profiles. Units are ms^{-1} for u_{*0} and Wm^{-2} for Q_{h0}

Run label	Sonic anemometer		Mean temperature and horizontal velocity profile	
	$u_{*0}(ms^{-1})$	$Q_{h0}(Wm^{-2})$	$u_{*0}(ms^{-1})$	$Q_{h0}(Wm^{-2})$
R1	0.29	85.0	0.25	82.3
R2	0.12	123.2	0.16	139.7
R3	NA	NA	0.29	20.4
R4	0.35	132.3	0.34	97.5
R5	0.23	14.3	0.22	11.6

the independent estimates computed from the sonic anemometer measurements, as shown by Table 2. The values for $u_\star$ and Q_h retained in the modelling are, respectively, quadratic and arithmetic averages of the 'sonic' and 'profile' estimates. The Obukhov length (L_{mo}) was accordingly derived as

$$L_{mo} = -\frac{u_\star^3}{k_v \frac{g}{T_0} \frac{Q_h}{\rho c_p}} \tag{11}$$

where k_v is the von Karman constant, g is the gravitational acceleration, T_0 is the reference temperature, ρ is the air density, c_p is the specific heat capacity of air at constant pressure. The roughness length z_0 was subsequently determined from a best fit between the observed mean velocity profile in the reference flow and a MOST parameterization of it based on the values of $u_\star$ and L_{mo}, determined as mentioned above. The mean ($\overline{\theta_0}$) and standard deviation ($\sigma_{\theta 0}$) of the wind direction were also calculated from the wind vane measurements. Note that throughout this paper, the overbar denotes the time average over the duration of an experimental run. All the micrometeorological statistics are presented in Table 1 for each run.

4.2 The wind flow about the shelterbelt

As an illustration, Fig. 8 presents the disturbance generated by the hedge (relative to the undisturbed values at the same vertical level upwind in the reference flow) in the mean horizontal wind field (panel a) and in the turbulent kinetic energy (TKE, panel b), as computed by the RANS model for the conditions of run R3. Note the significant decrease in the mean wind velocity in the region ($-3 < x/W < 4,\ z/H \leq 1$): mean wind reduction exceeds 50% within the shelterbelt and in its immediate wake. On the other hand the mean wind accelerates over the top of the windbreak; the accelerated zone stretches fairly high (above $z/H = 3$), but only in the region $0 < x/W < 1.5$, $1.2 < Z/H < 2.2$ does the speed increase exceed 10%. The turbulent kinetic energy field is also dramatically disturbed by the presence of the hedge. TKE is reduced by more than 50% in the lower downwind region of the shelterbelt, and this reduction extends into the wake to about $x/W = 1.4$. One observes also a large increase of the TKE (by more than 50%) along the upwind face and the top face of the hedge, where the wind shear is strongest. This enhanced TKE region extends and spreads downwind, and curves down to ground shortly after passing the shelterbelt.

Figure 9 shows the consistency between the modelled and the observed mean horizontal velocity perpendicular to the windbreak at heights $z/H = (0.15,\ 0.35,\ 0.55,\ 0.75,\ 0.95)$ along the upwind profile ($x/W = -0.60$) and the downwind profile ($x/W =$

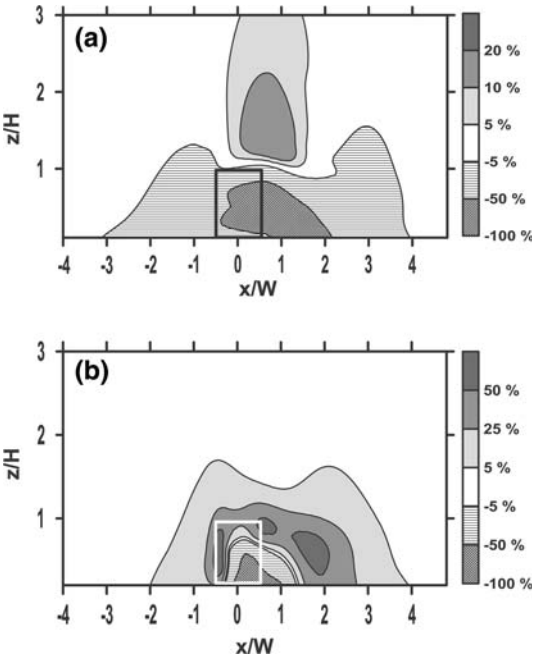

Fig. 8 Disturbance in the mean horizontal velocity (Panel a) and in the turbulent kinetic energy (Panel b), in percent relative to the undisturbed value upwind. The rectangle shows the outline of the maize belt of height H and width W. The meteorological conditions are those of run R3

0.60), for run R5. The close match, achieved by adjusting $c_d(z)$, suggests the mean wind speed is satisfactorily reproduced inside the hedge; unfortunately we have no measurements to check the model fields of the velocity variances, but these should have been qualitatively reasonable, since the inflow profiles of $\overline{u'^2}(z)$ etc. of the RANS model are equilibrium (1D) solutions held to lower and upper boundary values derived from the Monin–Obukhov universal relationship, $\overline{u'^2}/u_\star^2 = \phi_{uu}(z/L_{\mathrm{mo}})$.

4.3 Particle concentration and fluxes

Vertical profiles of concentration at entry to and exit from the maize belt are presented in Fig. 10. The standard deviation of the observed concentration relates to the deviation in the particle count of the 20 areas sampled on the particle trapping instrument's strips. In all the runs presented, the numerically simulated concentration profile at entry of the hedge matches perfectly the measurements, this being a constraint of the modelling: we remind the reader that we adjusted the source profile intensity so as to reproduce the measured concentration profile at entry of the maize belt. The upwind experimental concentration profiles have rather different shapes from one run to the next. However, in view of the expanded set of parameters governing heavy particle dispersion (as oppose to passive scalar dispersion), form similarity of the concentration field should not be expected. Examining this matter in more detail, we note Runs R1b, R3 and R4 display the same features, with upwind concentration peaking slightly below the source height ($H_S/H = 0.82$), and falling sharply with decreasing height below the peak. In those three runs, the far upstream horizontal wind component perpendicular to the hedge was fairly strong ($\overline{u}_{0H} = 2.74,\ 2.73,\ 4.26\,\mathrm{m\,s^{-1}}$ for runs R1b, R3 and R4, respectively). Therefore, the particle plume had little time

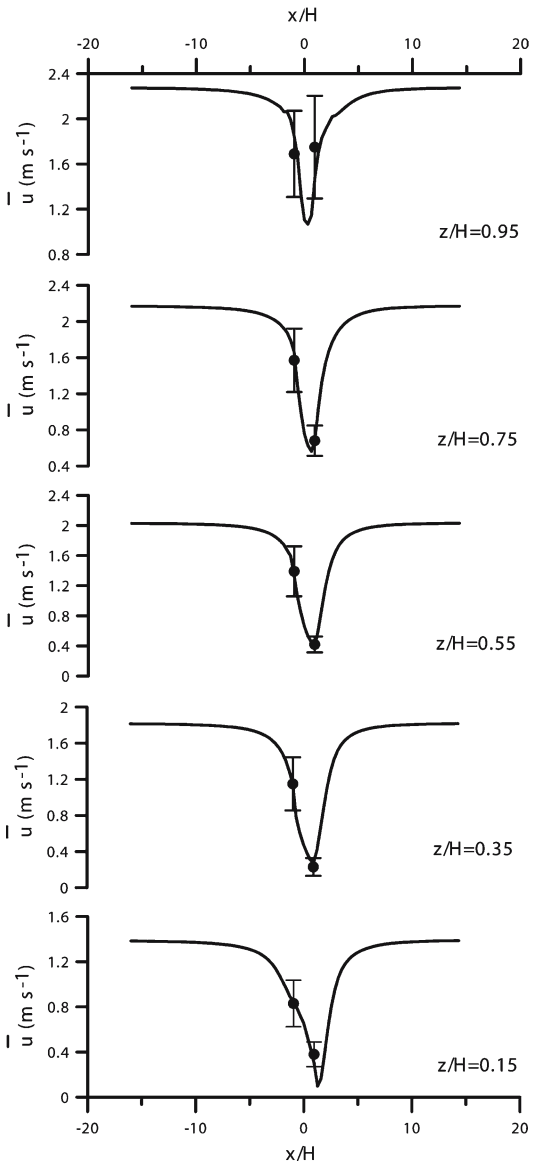

Fig. 9 Mean horizontal velocity perpendicular to the hedge, computed by the RANS model (curves) or measured experimentally (dots) during run R5, at five vertical levels: $z/H = 0.15, 0.35, 0.55, 0.75, 0.95$

to settle under gravity and to spread in the vertical before encountering the face of the shelterbelt. This explains why a concentration peak can be observed close to the level of the source. On the other hand in runs R1a and R5 one does not observe such a peak, although the wind conditions ($\overline{u}_{0H} = 2.74,\ 2.13\,\mathrm{m\,s^{-1}}$ for runs R1a and R5, respectively) were similar to those of runs R1b, R3 and R4. How can this be explained?

The results of run R1a are to be interpreted by considering the smaller size of the particles ($10 \leq d_\mathrm{p} \leq 25\ \mu\mathrm{m}$) relative to those of runs R1b, R3 and R4 for which particles were up to 50 μm in diameter. In effect, the positive mean vertical velocity

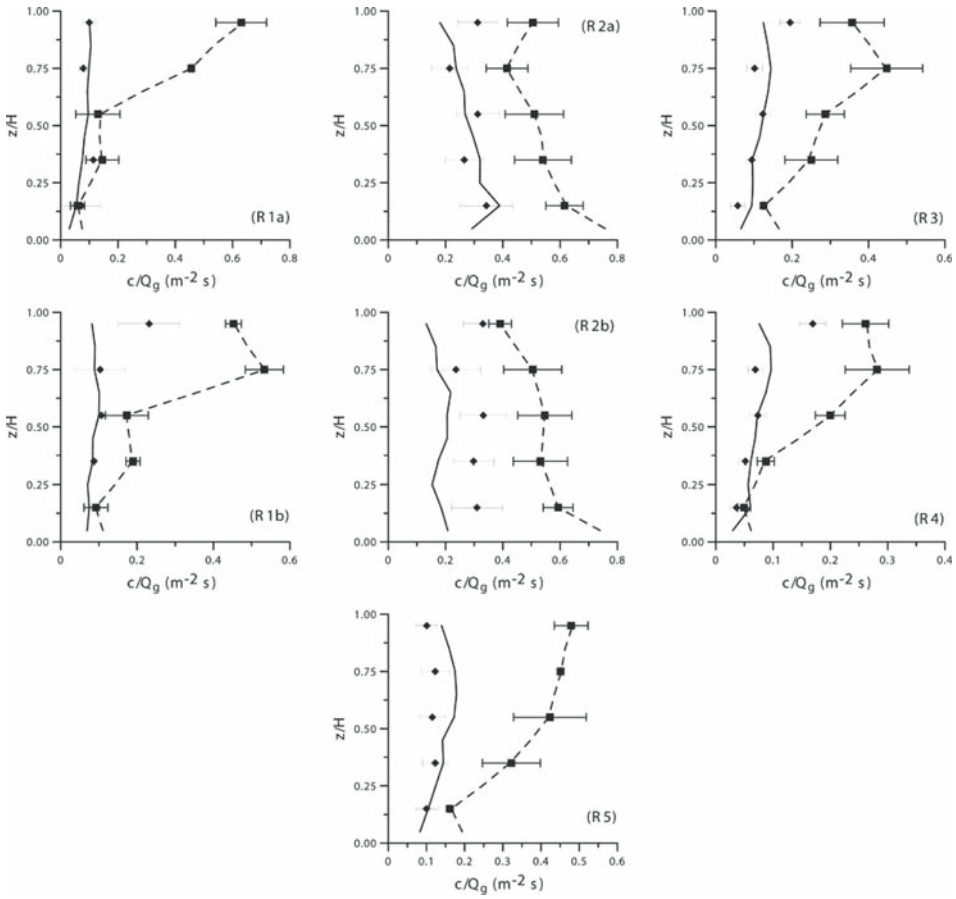

Fig. 10 Vertical profiles of concentration (normalized by the source intensity Qg) measured upwind at $x/W = -0.6$ (squares) and downwind at $x/W = 0.6$ (diamonds). The corresponding numerical simulation results are shown with dashed (upwind) and solid (downwind) curves. Note that the virtual source, placed at $x/W = -0.6$, was adjusted to fit the upwind concentration profile

upwind of the hedge overcomes the gravitational settling velocity of small particles. Neglecting velocity fluctuations, the average vertical displacement of a particle travelling from the source (at $x = x_S$) to the vertical plane ($x = x_1$) just upwind from the windbreak where concentrations were measured is approximated by an integral

$$\Delta z = \int_{x_S}^{x_1} \frac{\overline{w}(x,z) + w_g}{\overline{u}(x,z)}\, dx \tag{12}$$

along the particle path. Evaluating this expression from a computation of the RANS–LS model in the conditions of run R1a, we estimated that a 20-μm diameter particle would rise by 0.39 m above the source height $H_s/H = 0.82$ by the time it reaches the plane of the upwind measurement profile at $x = x_1$. In consequence the plume is lifted above the highest level of measurement ($z/H = 0.95$). This explains why one

does not observe a concentration peak in the concentration upwind profile of run R1a. As for the other runs, in R5 the source was placed higher than in the other runs ($H_s/H = 0.95$) and the plume mass centreline was too high for a concentration peak to be identified in the measurements. Finally, in runs R2a and R2b the concentration was fairly homogeneous on the inflow profile, a peculiarity associated with the significantly lighter winds than in the other runs ($\overline{u}_{0H} = 1.58\,\mathrm{m\,s^{-1}}$; $u_\star = 0.14\,\mathrm{m\,s^{-1}}$). Lower winds imply that particles have a longer time to spread before arriving at a given downwind distance, but also imply a smaller particle diffusivity. In the far field limit, and assuming a homogeneous velocity field, the variance in particle height after travel time t is

$$\sigma_z^2(t) = 2\sigma_w^2 T_L t \tag{13}$$

where T_L is the Lagrangian integral time scale and σ_w^2 is the vertical velocity variance. Note that $\sigma_w^2 \propto u_\star^2$ whereas $T_L \propto 1/u_\star$ and $t \propto 1/u_\star$. As a rough approximation then, particle spread σ_z^2 due to the turbulence does not depend on wind speed. However, there is another mechanism inducing spread, namely differential gravitational settling (i.e., faster settling of larger particles). In the lighter wind conditions of experiment R2, particles travel longer before reaching the hedge, and therefore spread more than in the other runs. According to Eq. 12, in the conditions of R2 a 10 μm particle (subject to gravitational settling and the mean flow only, i.e. turbulent fluctuations are artificially discarded) rises by 0.24 m by the time it reaches the windbreak, whereas a 50 μm particle drops by 0.84 m: differential gravitational settling accounts for a vertical spread of the order of 1 m.

Having addressed the variety of upwind concentration profiles encountered, we turn to the 'filtered' concentrations at the downstream face, assuming the degree of consistency of numerically simulated downwind concentrations with the measurements tests the ability of the model to reproduce particle filtration by vegetation. The match between observations and numerical simulations is very satisfactory for run R1a. In runs R1b, R2a, R3 and R4, the overall magnitude of concentration across the downwind profile is well reproduced, but concentration tends to be underestimated in the upper part near the top of the hedge. This trend is particularly marked in runs R1b and R4. Because the plants' individual heights were very variable, spanning $0.88 \leq z/H \leq 1.10$ (where H is the *mean* height), mean leaf area density in the upper part of the hedge computed from a sample of 15 plants may be locally unrepresentative, potentially explaining the discrepancy.

In run R2b the numerical simulation significantly underestimates the bead concentration over the whole profile. The reader should be aware that the impaction efficiency is highly variable in the range of particle size, velocity and leaf dimension applicable to this experiment. Should the velocity of a 30 μm particle heading towards a 40 mm wide leaf be overestimated by 20% (for example, $u = 0.6\,\mathrm{m\,s^{-1}}$ instead of $0.5\,\mathrm{m\,s^{-1}}$, the approximate velocity at the centre of the hedge in run R2), the impaction efficiency E_I of the particle would be overestimated by over 42%. The air flow is a component of the modelling that is subject to inaccuracy. Even though we have evidence that the mean horizontal velocity was well reproduced by the RANS model, one should keep in mind that the observations diplayed a large variability (See Fig. 9). In addition, the RANS model is known to be poor at computing velocity variances (Wilson 2004); this certainly would affect the accuracy of the instantaneous particle velocities calculated by the LS model. There are also uncertainties pertaining to the size distribution of the particles released at the 'virtual sources' in the modelling,

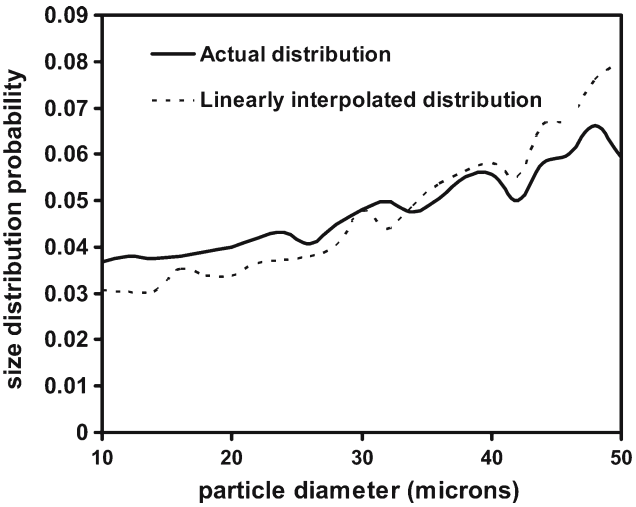

Fig. 11 Actual particle size distribution at $z/H = 0.6$, $x/W = -0.6$ (virtual source plane) versus distribution derived from linear interpolation between the distribution at the top and the bottom of the shelterbelt. The results are numerically simulated, when a line source is placed at $z/H = 0.82$, $x/W = -3.5$ releases particles of size uniformly distributed in the range 10–50 μm

which is linearly interpolated (with distance) between the distribution measured at ground and at the top of the shelterbelt. Figure 11 compares the actual size distribution, at $x/W = -0.6$ (plane of the virtual source) and $z/H = 0.6$, with the distribution derived from the linear interpolation method. The results shown are obtained by numerical simulation in the meteorological conditions of run R2, with a line source placed at $x/W = -3.5$, $z/H = 0.82$, which releases particles of size uniformly distributed in the range 10–50 μm. The graph shows that particles smaller than 33 μm are under-represented with the linear interpolation method (and correspondingly, particles larger than 33 μm are over-represented), with an error lying within 34%. In conditions pertaining to R2 ($u \approx 0.5\,\mathrm{m\,s^{-1}}$, 40 mm wide leaves), overestimating the size of a 30 μm particle by 5 μm results in an error of 80% in the impaction efficiency on the leaves.

Thus in view of the sensitivity of the impaction efficiencies to errors in the computed winds and in particle diameters, a substantial degree of error in the computed downwind (filtered) concentrations is inevitable. Nonetheless, overall the magnitude of the 'jump' (across the hedge) in the concentration profile has been quite well captured, with errors (relative to the concentration upwind from the windbreak) no larger than 24%, except in the upper region where the input values of $A(z)$ are dubious. We conclude that the LS model reproduces the concentration profiles reasonably satisfactorily, bearing in mind the questionable level of accuracy of the velocity statistics and of the particle size distribution provided to it.

Turning now to the rate of deposition on ground under the 'hedge', in Fig. 12 we compare the numerically simulated deposition flux integrated over the width of the maize belt against observations from runs R1b and R2b. The match is accurate within 14% and 35%, respectively, in runs R1b and R2b. In parallel are presented the observed and modelled horizontal particle fluxes carried by the mean wind flow across the vertical faces of the hedge (integrated over the height of the hedge), in

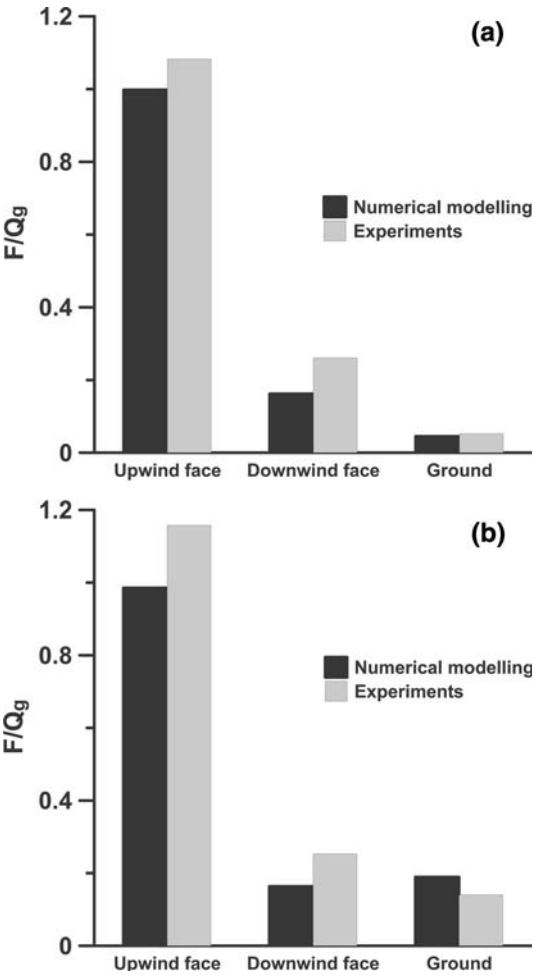

Fig. 12 30–50 μm particle fluxes ($m^{-1}\,s^{-1}$) normalized by the source intensity ($m^{-1}\,s^{-1}$) across the upwind face of the hedge, across the downwind face or onto ground for run R1b (panel a) and R2b (panel b). Comparison between experimental results and numerical simulations

order to show how they compare with ground deposition in terms of magnitude. This horizontal flux is calculated as

$$F = \int_0^H \overline{u}(z)\,\overline{c}(z)\mathrm{d}z \tag{14}$$

where $\overline{u}$ is the mean horizontal velocity perpendicular to the hedge, and $\overline{c}$ is the average concentration. The mismatch between numerical and experimental results of the horizontal flux upwind is fairly small (8% in run R1b and 15% in run R2b). Effectively, the discrepancy in the upwind flux stems from inaccuracies in the mean horizontal wind only, since concentration is forced to reproduce the observations along the upwind vertical profile. Errors of about 35% occur at the downwind profile; larger discrepancies (than upwind) are not surprising as they result from inaccuracies in both the input horizontal wind velocity and the modelling of particle dispersion. Again, these discrepancies seem tolerable in view of the suspect accuracy of the velocity statistics and the particle size distribution provided to the LS model and the high sensitivity

of the model's response to input errors. The deposition flux at the ground turns out to represent only a small portion (5% and 12% in runs R1b and R2b, respectively) of the horizontal particle flux carried by the mean wind entering the maize belt. This means that a large fraction of the incoming particles are deposited on the vegetation, and/or exit the maize belt across the upper surface of the hedge.

4.4 Comparison with the treatment of entrapment by Raupach et al. (2001)

The theory developed by Raupach et al. (2001, referred to as R2001 in this section) is satisfyingly simple, fixing the transmittance of the windbreak σ in terms of an economical set of parameters, viz.

$$\sigma = \frac{\overline{c}_2}{\overline{c}_1} \approx \eta^{m E_I} \tag{15}$$

where (as earlier) $\overline{c}_1$ and $\overline{c}_2$ are, respectively, the mean particle concentrations immediately upwind and downwind from a windbreak and the optical porosity η is related to the projection of the area density A (m^{-1}) onto a vertical plane parallel to the shelterbelt,

$$\eta = e^{-A W}. \tag{16}$$

As earlier E_I is the efficiency of impaction on vegetation elements, while $m = L/W$, the 'meandering factor', is the ratio of the pathlength (L) of a particle's (meandering) trajectory across the shelterbelt, to the straightline width (W).

Because the R2001 theory is enticing for its simplicity, it is worthwhile to investigate whether it compares satisfactorily with the results of the present numerical model despite its strong assumptions, viz. (a) neglect of deposition on horizontal surfaces (ground and vegetation), (b) neglect of particle flux across the upper boundary of the windbreak, (c) neglect of rebound and (d) constant horizontal velocity '$V_\mathrm{b}(z)$' across the width of the shelterbelt. The comparison was performed on the natural hedge described in Sect. 2 for 33-μm diameter particles ($w_\mathrm{g} = 82\,\mathrm{mm\,s}^{-1}$) carried by a normally incident flow, in a neutrally stratified atmosphere with friction velocity (defined far upwind in the undisturbed flow) $u_\star = 0.3\,\mathrm{m\,s}^{-1}$ and a roughness length $z_0 = 0.01\,\mathrm{m}$. We computed the overall transmittance across the windbreak as

$$\sigma = \frac{\int_0^H \overline{c}_2(z)\mathrm{d}z}{\int_0^H \overline{c}_1(z)\mathrm{d}z} \tag{17}$$

by applying the treatment of R2001 along a series of mean streamlines at different heights. To this end we estimated $\overline{c}_1(z)$ from a RANS-LS simulation run in the conditions described above, and $E_\mathrm{I}(z)$, $m(z)$ and $\eta(z)$ were estimated following R2001 (their Sect. 2.1 for E_I, Sect. 2.2 for η and Appendix for m) from the canopy vegetation measurements and the velocity statistics computed by the wind flow model at the centre of the shelterbelt. For comparison, the corresponding numerical prediction by the far more intricate model described in Sect. 3 was computed as

$$\sigma = \frac{N_\mathrm{out}}{N_\mathrm{in}} \tag{18}$$

where N_in is the number of particles entering the windbreak through the upwind vertical face, and N_out is the number of particles flowing out through the top

(horizontal) or downwind (vertical) boundaries of the hedge, from a simulation of 10,000 trajectories. Recalling that the numerical simulation was not intended to reproduce any experimental run, the source was defined to conveniently produce a fairly uniform concentration profile at entry of the hedge: it was positioned upwind of the shelter belt at $X_S/W = -1.5$, and spanned in the vertical the region $0 \leq z \leq 2H$. It released particles of 33 μm in diameter (for comparison purposes) at a uniform rate along its vertical span, i.e., uniform source distribution.

The transmittance predicted by the analytical approach (Eq. 17), $\sigma = 0.80$, was quite close to the numerical model result, $\sigma = 0.83$. Taken at face value, this result is very surprising. One might have expected that the assumption (a) (neglect of deposition on horizontal surfaces), which would logically cause a reduced toll of deposition, would lead to an *over*estimation of the transmittance by the analytical theory. However, assumptions (b) and (c) induce counter-balancing effects. Indeed, not accounting for particle escape across the top face (shown later in Sect. 4.5) causes an overestimation of the particle mean path length in the shelterbelt (equivalently an overestimation of the meandering factor m), leading to a smaller transmittance. The neglect of rebound has qualitatively the same effect.

We assessed the magnitude of the counter-balancing errors induced by the assumptions of the R2001 treatment, by comparing the transmittance computed when applying these assumptions artificially in the numerical model with the reference result where simplifications are not made (i.e., $\sigma = 0.83$). Skipping rebound (c.f. assumption c) results in a transmittance reduced by 10%. Not allowing deposition on ground and horizontal surfaces in the vegetation (c.f. assumption (a)) has even less impact (transmittance increased by 3%). When assumptions (a) and (c) are applied together in the numerical simulations, the computed transmittance is $\sigma = 0.77$, a figure extremely close to the transmittance predicted by the analytical treatment (Eq. 17). This suggests that the remaining assumptions (b) and (d) cause minor error, unless their respective impacts are large and in opposite directions. This is unlikely. Indeed, the 'global' meandering factor m_G calculated by the numerical model (from the ensemble average of particle path length in the vegetation when no deposition occur, computed from all particles entering the hedge) is only slightly smaller than the values $m_{R2001}(z)$ calculated following R2001: $m_G = 0.96$ whereas $m_{R2001}(z) = 1.07 \pm 0.04$. However, it is worthwhile noting that in the overall figure for m_G hides large vertical inhomogeneities. In effect $m(z)$, the meandering factor of particles entering the hedge at height z, computed with RANS–LS simulations, ranges from 0.3 by the top of the shelterbelt (illustrating that particles escape through the top horizontal face) to 1.4 by the ground, whereas the values calculated from R2001 are in the range $1.03 < m_{R2001}(z) < 1.12$ only. In turn R2001 significantly underestimates deposition in the lower part of the windbreak, whereas it significantly overestimates it in the upper part.

In summary, the analytical treatment of R2001 seem very satisfactory in our situation, in the sense that it yields a global transmittance very similar to the far more complex numerical approach. However, this result is ambiguous and misleading, for it occults compensating errors. Consequently, it cannot be extrapolated to any other experimental regimes, where the non-adequacy of the assumptions (in particular the neglect of particle escape through the top face) may reveal and translate into much larger error.

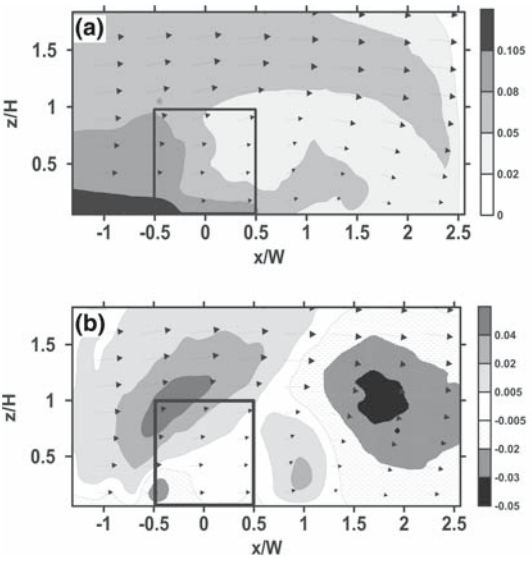

Fig. 13 Fields of particle concentration (Panel a) and vertical fluxes (Panel b) about the maize belt (rectangle). Both concentration and fluxes are normalized by the source strength. The arrows show the mean wind vector field, computed for the conditions of run R3. The source is placed at $x/W = -1.5$ and releases 33 μm particles ($w_g = 82\,\mathrm{mm\,s^{-1}}$) uniformly along its vertical $2H$ span

4.5 Particle dispersion patterns

To understand the influence of a thick natural shelterbelt on particle dispersion, we need to look not only at processes within the hedge, but also in its vicinity. To this end Fig. 13 shows a synthetic particle concentration field, as modelled by the LS model coupled with the RANS wind flow model in the conditions of run R3. The grey shaded contours represent the concentration normalized by the source intensity, and the vectors show the mean velocity field. When looking at the concentration profile immediately downwind of the uniform source, note that the concentration increases closer to ground, where the wind velocity decreases. In other words, particles tend to accumulate in low wind velocity regions. Marching downwind across the shelterbelt a clear decrease in particle concentration is identifiable, due to particle deposition onto vegetation. However, the decrease is more marked in the upper part of the hedge. Figure 13b shows the vertical flux of particles (superposed on the mean wind field vector map) for the same conditions as in Fig. 13. Note the strong outflow of particles across the upper (horizontal) boundary of the thick hedge, seen by the grey shades representing a positive flux. This outflow depletes particles in the upper region of the hedge, thus explaining why concentration decreases faster than in the bottom region. Interesting features are identifiable downwind of the hedge too. The grey patch (positive flux) seen immediately downwind of the shelterbelt in Fig. 13b shows an upwelling of particles, driven by a large positive vertical wind velocity. Further downwind, the mean vertical wind velocity becomes negative, causing particles to sink. The downwash flux is most pronounced at height $z/H \approx 1$, where concentration is highest (at this level downwind). Those characteristics of the particle vertical flux field translate into distortions of the particle plume downwind of the shelterbelt as seen on the concentration map (Fig. 13).

The numerical simulations described above pertain to 33 μm particles, and it is worthwhile to investigate how particles of different sizes respond to the disturbance of a shelterbelt. Figure 14 shows the evolution of the proportion of particles of three

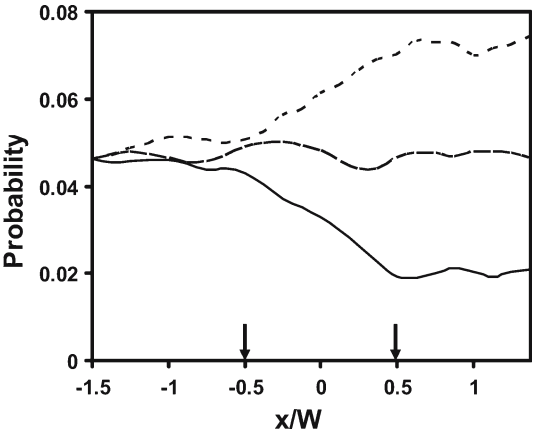

Fig. 14 Proportion of particles of diameter 10 ± 1 μm (dotted curve), 30 ± 1 μm (dashed curve) and 50 ± 1 μm (solid curve) along a horizontal transect at $z/H = 0.6$ across the shelterbelt located at $-0.5 \leq x/W \leq 0.5$ (arrows indicate its limits). The source is placed at $x/W = -1.5$; it is spatially uniform in the vertical and is also uniformly distributed in size, in the range $9 \leq d \leq 51$ μm. The meteorological conditions are those of run R3

different sizes (10 ± 1, 30 ± 1 and 50 ± 1 μm) along a horizontal transect crossing the shelterbelt. The results are obtained with numerical simulations identical to the ones described in Sect. 4.4, except that the source released particles uniformly distributed in size in the range 9–51 μm (as opposed to particles of diameter 33 μm). The graph indicates that the size distribution drifts when marching downwind, with the 10 μm particles being increasingly represented to the detriment of the 50 μm particles. This trend starts immediately after particle release, and is due to faster gravitational settling of larger particles. The distribution drift accelerates sharply in the region of the shelterbelt ($-0.5 \leq x/W \leq 0.5$). As we mentioned in Sect. 4.3, the efficiency of impaction of particles on vegetation is highly sensitive to particle size, with larger particles impacting more. As a consequence, smaller particles statistically deposit less onto vegetation. In other words, a shelterbelt preferentially filters large particles, which explains the drift of the size distribution towards small particles. This pattern is visible also on Fig. 15, a contour plot of the deviation of the median size of particles that have a uniform size distribution at source. The median size decreases as the plume crosses vegetation, due to preferential deposition of large particles. The deviation reaches a maximum (in absolute value) downwind from the windbreak at about $x/W \approx 0.8$, where deposition onto vegetation does not occur anymore. The sharp depletion in large particles is due to the enhanced gravitational settling in this region where the wind reduction is strongest. Further downwind, the updraft partially annihilates this depletion.

The particle mass budget across the shelterbelt becomes understandable in the light of the dispersion patterns described above. Figure 16 shows the 'fate' of 33 μm particles entering the shelterbelt across its upwind (x_1) face.[7]. More than a third of those particles are deposited onto vegetation, and another third flow out across the top horizontal boundary ($z = H$). Only a small portion (less than 10%) are deposited onto the ground, and the remainder (about 25%) flow out across the downwind (x_2) face. With larger particles, the fraction depositing onto the ground grows to the detriment of the outflux across the top boundary. In a normally incident flow (as in

[7] The terms of the mass budget do not add precisely to 100% (Fig. 16) because particles may enter the shelterbelt volume across the top face, without traversing the upwind side, and thereby contribute to the mass budget; but the normalizing flux is that entering across the upwind face.

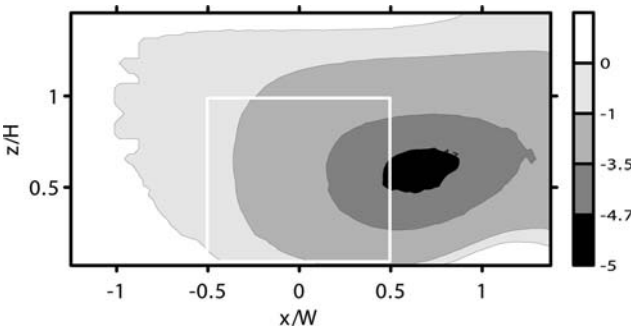

Fig. 15 Deviation in the median particle size, in μm, calculated by numerical simulation. The source is spatially uniform along the vertical, and releases particles with diameters uniformly distributed in the range 9–51 μm, in a wind field consistent with meteorological conditions of run R3

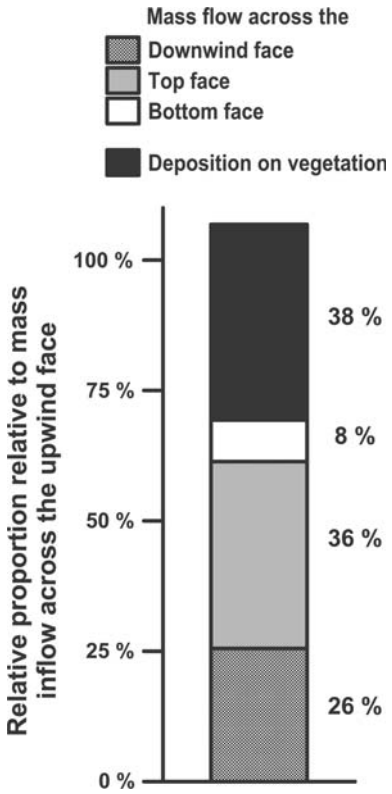

Fig. 16 Particle mass budget in the shelterbelt (numerical simulation). The source is placed at $x/W = -1.5$ and releases 33 μm particles ($w_g = 82\,\mathrm{mm\,s^{-1}}$) uniformly along its vertical $2H$ span. The particles are carried in a wind flow computed for the conditions of run R3

the case in the conditions described in Sect. 4.4), the particle's trajectory path length inside vegetation is statistically shorter, and deposition is accordingly smaller. However, the particle budget terms remain overall qualitatively similar. As a consequence, the fluxes across the horizontal faces of the thick hedge (i.e., deposition flux at the ground and the vertical flux across the top boundary) cannot be neglected, as they amount to more than 40% of the particle flux entering the shelterbelt. These findings

confirm that the theory of Raupach et al. (2001) is not a satisfactory approximation for the entrapment of particles by thick windbreaks.

We close this section by noting that the simulations indicate a rather minor role of velocity fluctuations in particle transport about the windbreak, a factor which, if generally valid, may permit helpful simplification in any future effort to construct a simpler entrapment theory than the type of detailed numerical simulation we have employed in this paper. Figure 17 indicates the horizontal fluxes of particles across the hedge's inflow (x_1, Panel a) and outflow (x_2, Panel b) faces are carried essentially by the mean horizontal wind: in the conditions of run R3, at most about 15% of the particles are carried by the turbulent wind field. In other words the flux of particles transported by the mean wind, which can be easily measured experimentally (with wind cups and particle trapping instruments for example), is a useful first-order approximation of the total flux. It is interesting to notice that the turbulent flux across

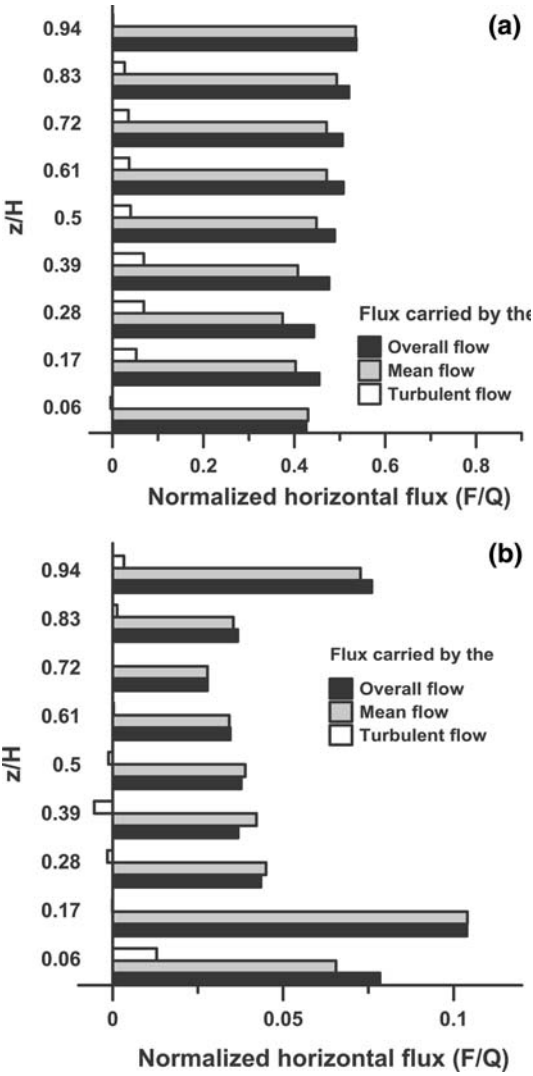

Fig. 17 Computed horizontal fluxes of particles carried by the mean velocity field (in grey shade), the turbulent velocity field (in white) or by the overall wind field (in black), across the upwind face of the shelterbelt (Panel a) or the downwind face (Panel b). The source is placed at $x/W = -1.5$ and releases 33 μm particles ($w_g = 82\,\mathrm{mm\,s^{-1}}$) uniformly along its vertical $2H$ span. The particles are carried in a wind flow computed for the conditions of run R3

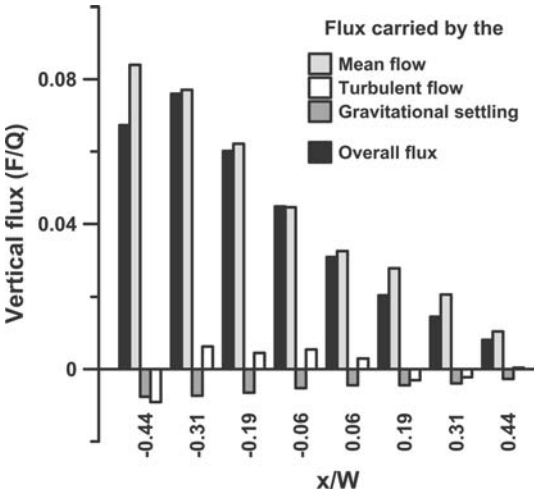

Fig. 18 Computed vertical flux across the top boundary of the shelterbelt, carried by the mean flow (in light grey), the turbulent flow (in white) or the gravitational settling (in dark grey). The overall flux (in black) is the sum of all the others

the downwind face remains essentially zero at all points along the vertical. This is consistent with the concentration field (Fig. 13). Indeed, concentration increases both to windward and to leeward from the hedge's downwind side; in turn the horizontal gradient of concentration is likely to be close to zero across this downwind face, causing the turbulent flux to vanish (if one may hazard to invoke the gradient-diffusion paradigm). Only near ground does the turbulent flux become significant, where the concentration gradient and turbulent intensity are high. Figure 18 presents the vertical flux across the top (horizontal) face of the hedge. Clearly, both the turbulent flux and the flux driven by the gravitational settling velocity remain minor relative to the flux carried by the mean wind.

5 Conclusion

We have focused on the role of a shelterbelt as a particle filter, and therefore on trajectories *within* the vegetation, taking a few specific cases of the meteorological conditions and a single example of the windbreak dimension, vegetation density, leaf orientation and size. What has been proven is that entrapment may be described reasonably well by RANS–LS modelling, with relative errors in the concentration jump across the hedge no larger than about 25%. However that computational approach is burdensome and inconvenient, accessible only to specialized individuals or teams. The simple analytical approach of Raupach et al. (2001) is not appropriate to capture particle filtering by a thick natural shelterbelt. For rapid practical calculations, a generalized analytical description is needed. Although we offer no progress in that regard, the present data highlight the want of, and hopefully will serve to test, a simplified theory.

As well as filtering the airstream, obviously a windbreak perturbs the paths of particles in its general vicinity. It would be interesting to investigate the overall impact of a shelterbelt, acting as both a filter and as a windbreak, on the aerial transportation and deposition of particles, at a scale of tens to hundreds and even thousands of metres. Studying the sensitivity of the dispersion patterns to the meteorological conditions (friction velocity, thermal stability, wind obliquity) and to the specifics of the vegetation might allow us to determine in what conditions particles are most vulnerable to

long distance drift, and to suggest an optimal design in terms of geometry, vegetation density and leaf size. Those issues will be addressed in future work.

Acknowledgements Funding for these studies has been provided in part by the Natural Sciences and Engineering Research Council of Canada (NSERC), and the University of Alberta. We would like to thank Brigitte Durand for her invaluable support during and after the experiments, and in particular for carrying out the optical count of particles collected by the particle trapping instruments.

References

Aylor DE (1982) Modeling spore dispersal in a barley crop. Agric Meteorol 26:215–219
Aylor DE (1990) The role of intermittent wind in the dispesal of fungal pathogens. Annu Rev Phytopathol 28:73–92
Aylor DE, Flesch TK (2001) Estimating spore release rates using a lagrangian stochastic simulation model. J Appl Meteorol 40:1196–1208
Bouvet T, Wilson JD, Tuzet A (2006) Observation and modelling of heavy particle deposition in a windbreak flow. J Appl Meteorol Climatol 45:1332–1349
Csanady GT (1963) Turbulent diffusion of heavy particles in atmosphere. J Atmos Sci 20:201–208
Dahneke BJ (1971) Capture of aerosol particles by surfaces. J Colloid Interface Sci 37:342–353
Dahneke BJ (1975) Kinetic-theory of escape of particles from surfaces. J Colloid Interface Sci 50:89–107
Dong Z, Wang X, Liu L (2000) Wind erosion in arid and semiarid China: An overview. J Soil Water Conserv 55:439–444
Finnigan JJ (2000) Turbulence in plant canopies. Ann Rev Fluid Mech 32:519–571
Jarosz N, Loubet B, Durand B, McCartney A, Foueillassar X, Huber L (2003) Field measurements of airborne concentration and deposition rate of maize pollen. Agric For Meteorol 119:37–51
Klein EK, Lavigne C, Foueillassar X, Gouyon PH, Laredo C (2003) Corn pollen dispersal: Quasi mechanistic models and field experiments. Ecol monogr 73:131–150
Maber J (1998) Spray drift and Shelter. A brief summary of the effects of shelter on spray drift, Lincoln technology, Hamilton, New Zealand, 5 pp
May KR, Clifford R (1967) The impaction of aerosol particles on cylinders, spheres, ribbons and discs. Ann Occup Hyg 10:83–95
Oldeman LR, Hakkeling RTA, Sombroek WG (1991) World map of the status of human-induced soil degradation. An explanatory note, revised version, United Nations Environment Program (UNEP) and International Soil Research Information Center (ISRIC), Wageningen, Netherlands, 35 pp
Paw UKT (1983) The rebound of particles from natural surfaces. J Colloid Interface Sci 93:442–452
Polhemus F (1993) 3SPACE Fastrak user's manual. F. Polhemus Inc., Colchester, VT, 158 pp
Rao KS, Wyngaard JC, Cote OR (1974) Local advection of momentum, heat, and moisture in micrometeorology. Boundary-Layer Meteorol 7:331–348
Raupach MR, Woods N, Dorr G, Leys JF, Cleugh HA (2001) The entrapment of particles by windbreaks. Atmos Environ 35:3373–3383
Raupach MR (2002) Diffusion of heavy particles in a turbulent flow. In: Raats PAC, Smiles DE, Warrick AW (ed) Environmental mechanics: water, mass and energy tranfer in the biosphere (The Philip Volume), Geophysical Monograph 129, Amer Geophys Union, Washington DC, pp 301–316
Shaw DL (1988) The design and use of living snow fences in North America. Agric Ecosystems Environ 22/23:351–362
Shaw DT (1978) Fundamentals of aerosol science. Wiley-Interscience Publications, New York, 372 pp
Thomson DJ (1987) Criteria for the selection of stochastic models of particle trajectories in turbulent flows. J Fluid Mech 180:529–556
Ucar T, Hall FR (2001) Windbreaks as a pesticide drift mitigation strategy: a review. Pest Manag Sci 57:663–675
Waggoner PE, Taylor GS (1958) Dissemination by atmospheric turbulence: spores of Peronospora tabacina. Phytopathology 48:46–51
Wilson JD (2000) Trajectory models for heavy particles in atmospheric turbulence: comparison with observations. J Appl Meteorol 39:1894–1912

Wilson JD (2004) Oblique, stratified winds about a shelter fence. Part II: comparison of measurements with numerical models. J Appl Meteorol 43:1392–1409
Wilson JD, Flesch TK, Harper LA (2001) Micro-meteorological methods for estimating surface exchange with a disturbed windflow. Agric For Meteorol 107:207–225
Woods N, Craig IP, Dorr G, Young B (2001) Spray drift of pesticides arising from aerial application in cotton. J Environ Qual 30:697–701
Xu M, Willeke K (1993) Impaction and rebound of particles at acute incident angles. Aerosol Sci Tech 18:143–155